Spatiotemporal variations of dissolved organic carbon and carbon monoxide in first-year sea ice in the western Canadian Arctic

Guisheng Song,[1] Huixiang Xie,[1] Cyril Aubry,[1,2] Yong Zhang,[1,3] Michel Gosselin,[1] C. J. Mundy,[1] Benoît Philippe,[1] and Tim N. Papakyriakou[4]

Received 6 December 2010; revised 22 July 2011; accepted 26 August 2011; published 9 November 2011.

[1] We monitored the spatiotemporal progression of dissolved organic carbon (DOC) and carbon monoxide (CO), along with general meteorological, hydrographic, and biological variables, in first-year sea ice in the western Canadian Arctic between mid-March and early July 2008. DOC and CO concentrations fluctuated irregularly in surface ice, but followed the concentration of ice algae in bottom ice, i.e., low at the start of ice algal accumulation, highly enriched during the peak-bloom and early post-bloom, and depleted again during sea ice melt. Vertical profiles of DOC and CO typically decreased downward in early spring and were variable in the melting season. In the presence of high bottom ice algal biomass in mid-spring, DOC and CO exhibited high concentrations in the bottom (DOC: 563 ± 434 μmol L^{-1}; CO: 82.9 ± 84 nmol L^{-1}) relative to the surface (DOC: 56 ± 26 μmol L^{-1}; CO: 16.8 ± 7 nmol L^{-1}). Landfast ice contained higher levels of DOC and CO than drifting ice. Cruise-mean DOC and CO inventories in sea ice were 87 ± 51 mmol m^{-2} and 13.9 ± 10 μmol m^{-2}, respectively. Net productions of DOC and CO linked to the ice algal bloom were assessed to be 75 mmol m^{-2} and 13.2 μmol m^{-2}. Sea ice in the study area was estimated to contribute 7.4×10^7 moles of CO a^{-1} to the atmosphere. This study suggests that sea ice plays important roles in the cycling of organic carbon and trace gases.

Citation: Song, G., H. Xie, C. Aubry, Y. Zhang, M. Gosselin, C. J. Mundy, B. Philippe, and T. N. Papakyriakou (2011), Spatiotemporal variations of dissolved organic carbon and carbon monoxide in first-year sea ice in the western Canadian Arctic, *J. Geophys. Res.*, *116*, C00G05, doi:10.1029/2010JC006867.

1. Introduction

[2] Sea ice influences the carbon cycle in polar oceans through modulating the transmission of light available for sea ice and water column primary production and photo-oxidation and by providing a habitat for a variety of organisms. It has been estimated that ice algae contributes 3–25% of the total primary production in seasonally ice-covered Arctic seas [*Legendre et al.*, 1992] and > 50% in the perennially ice-covered central Arctic Ocean [*Gosselin et al.*, 1997]. Biological processes involving ice algae produce dissolved organic carbon (DOC) and hence enrich it in bottom sea ice relative to underlying seawater [*Bunch and Harland*, 1990; *Gosselin et al.*, 1997; *Smith et al.*, 1997] despite exclusion of organic constituents during ice formation [*Giannelli et al.*, 2001; *Belzile et al.*, 2002; *Amon*, 2004]. DOC production makes up ~40% of the total organic carbon fixation by ice algae [*Gosselin et al.*, 1997; *Smith et al.*, 1997], demonstrating that organic carbon production can be seriously underestimated if the dissolved fraction is ignored. Understanding the distribution of DOC in sea ice and its seasonal variability, which remains poorly documented, is therefore critical for establishing links between DOC cycling and ecological functions of ice microorganisms.

[3] In addition to its role in organic carbon cycling, sea ice is also involved in the production or destruction of certain climatically and biogeochemically reactive trace constituents. For example, carbon monoxide (CO) [*Xie and Gosselin*, 2005] and hydrogen peroxide [*Klánová et al.*, 2003; *King et al.*, 2005] are generated while chlorine dioxide [*Pursell et al.*, 1995] and dimethylsulfide [*Hellmer et al.*, 2006] are decomposed in sea ice. Both sea ice and open seas can release CO to the atmosphere where it regulates the oxidizing capacity and acts as an indirect greenhouse gas through its reaction with the hydroxyl radical [*Watson et al.*, 1990; *Thompson*, 1992]. As the second most abundant and most precisely measured carbon photoproduct in the ocean, CO plays a crucial role in chromophoric dissolved organic matter (CDOM) photochemistry [*Miller and Zepp*, 1995; *Mopper*

[1]Institut des sciences de la mer de Rimouski, Université du Québec à Rimouski, Rimouski, Québec, Canada.
[2]Now at Département de biologie et Centre d'études nordiques, Université Laval, Québec, Québec, Canada.
[3]Key Laboratory of Coastal Zone Environmental Processes, Yantai Institute of Coastal Zone Research, Chinese Academy of Sciences, Yantai, China.
[4]Centre for Earth Observation Science, Department of Environment and Geography, University of Manitoba, Winnipeg, Manitoba, Canada.

0148-0227/11/2010JC006867

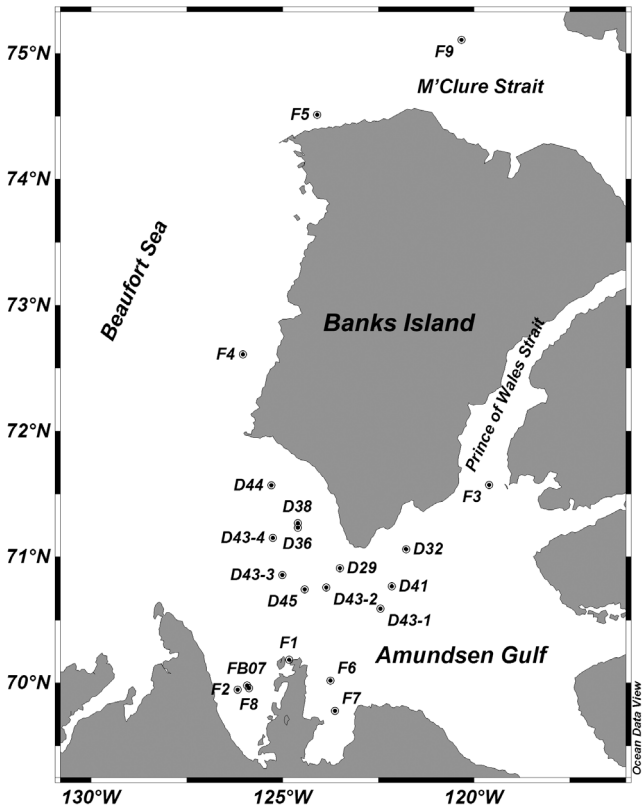

Figure 1. Map of sea ice sampling stations. Station symbols starting with D signify drifting ice and F signify landfast ice. This map was constructed using the online software of Ocean Data View (R. Schlitzer, 2010, unpublished data, http://odv.awi.de).

and Kieber, 2000]. CO also serves as potential carbon and energy sources for certain marine microbes [*King and Weber*, 2007; *Moran and Miller*, 2007]. Its short turnover times (usually < 1 d), mainly resulting from rapid microbial oxidation [*Conrad et al.*, 1982; *Zafiriou et al.*, 2003; *Xie et al.*, 2005], make CO an excellent tracer for modeling upper-ocean mixing dynamics [*Doney et al.*, 1995; *Kettle*, 2005]. In spite of extensive CO surveys in open oceans [*Conrad et al.*, 1982; *Bates et al.*, 1995; *Zafiriou et al.*, 2003, 2008; *Stubbins et al.*, 2006], information on CO in sea ice is scarce and incomplete. *Swinnerton and Lamontagne* [1974] briefly reported the observation of CO enrichment in Antarctic sea ice relative to open surface seawater. *Xie and Gosselin* [2005] collected a limited number of vertical profiles of CO concentration ([CO]) in landfast sea ice during the ice algal bloom season in Franklin Bay, western Canadian Arctic. [CO] profiles typically exhibit minima in the middle and increasing concentration toward the surface and bottom with particularly strong elevations at the bottom. Based on laboratory evidence, *Xie and Gosselin* [2005] suggested that this distribution was a function of CO photoproduction from CDOM in sea ice. However, these [CO] profiles were obtained over a narrow time span (11 d) and only at one site. Field measurements on larger time and space scales are required to better understand the seasonal and spatial variability of sea ice [CO] distribution, to constrain its source strength, and to evaluate its flux to the overlying atmosphere.

[4] Here we report measurements of DOC and CO concentrations in full-length sea ice cores collected in the western Canadian Arctic, covering both landfast and drifting ice and spanning from late winter to mid-summer. We assess the DOC and CO inventories and their net productions in sea ice and evaluate the contribution of sea ice to atmospheric CO. Results from this study improve our understanding of the roles of sea ice in marine organic carbon and trace gas cycling.

2. Methods

2.1. Meteorology and Hydrology

[5] The field campaign was carried out in the southeastern Beaufort Sea, including the Amundsen Gulf, Prince of Wales Strait, the coastal shelf west of Banks Island, and M'Clure Strait, during the 2007–2008 International Polar Year–Circumpolar Flaw Lead (IPY–CFL) system study aboard the icebreaker CCGS *Amundsen* [*Barber et al.*, 2010]. A meteorological tower mounted at the bow of the CCGS *Amundsen* was used to monitor shortwave radiation (285–2800 nm, PSP^{TM}, Eppley), photosynthetically active radiation (PAR, 400–700 nm, PARLite^{TM}, Kipp & Zonen), and air temperature (Vasaila HMP45C212, Campbell Scientific) at 1-min intervals.

[6] All sea ice sampling was conducted on first-year drifting and landfast sea ice from 17 March to 6 July 2008 (Figure 1). In the case of drifting ice, the ship drifted with the same ice floe for a certain period of time and then repositioned to the next ice floe. Sampling usually started around 9 a.m. and lasted for ~1 h. Some stations were sampled 2–4 times, often 3 d apart (Table 1). When on site, a moderate snow depth (typically < 5 cm; Table 1) was located. Numerous ice cores were extracted using a manually operated MARK II coring system (9 cm in diameter, Kovacs Enterprises). Following ice core extraction, the ice thickness and freeboard were measured. Sea ice temperature measurements were conducted on one of the ice cores immediately after extraction. Ice temperature was measured at 10 cm intervals using a handheld drill and a temperature sensor coupled with a stainless steel NTC food probe (IP65, Testo). The thermometer had a 0.001 reading resolution and an accuracy of ±0.05°C. Thawed ice cores collected for CO and DOC analyses (section 2.3) were used to determine sea ice salinity profiles using a WTW 330i conductivity meter with an accuracy of ±0.5%.

2.2. Chlorophyll *a*

[7] At each sampling site, one of the extracted ice cores was used for determination of chlorophyll *a* concentration ([Chl *a*]). From the bottom upwards, the ice core was consecutively cut into 3, 7, and 10 cm thick ice sections followed by 20 cm thick sections until reaching the surface section, which was variable in thickness. The ice sections were immersed in 0.2 μm-filtered seawater and left in the dark within isothermal containers overnight (12–14 h) to melt. The addition of filtered seawater (~3:1 filtered seawater to ice melt dilution) was intended to reduce osmotic stress-induced artifacts [*Garrison and Buck*, 1986]. Subsamples from the diluted meltwater were filtered onto duplicate GF/F filters (Whatman). The filters were then placed in 10 mL of 90% acetone in scintillation vials for at

Table 1. Sampling Dates, Locations, and Corresponding Sea Ice Conditions

Date	Station	Coordinates		Snow Depth (cm)	Ice Thickness (cm)	Freeboard[a] (cm)
		Latitude (N)	Longitude (W)			
17 Mar	D29	70°54.6′	123°30.0′	4.0	135	13
22 Mar	D32	71°3.7′	121°46.7′	3.5	149	9
25 Mar	D33-1	71°3.8′	121°47.2′	3.5	145	10
28 Mar	D33-2	71°3.8′	121°47.2′	3.5	149	10
31 Mar	D33-3	71°3.8′	121°47.2′	4.0	154	14
6 Apr	D36-1	71°16.0′	124°24.0′	2.5	160	12
9 Apr	D36-2	71°14.0′	124°36.0′	1.0	72	6
11 Apr	D38	71°16.0′	124°36.0′	2.0	124	12
16 Apr	D41	70°46.0′	122°9.0′	4.5	131	11
26 Apr	D43-1	70°35.3′	122°26.5′	4.5	135	12
29 Apr	D43-2	70°45.5′	123°51.4′	4.5	135	11
2 May	D43-3	70°51.3′	125°0.4′	4.5	141	12
5 May	D43-4	71°9.1′	125°15.2′	5.0	137	10
8 May	F1-1	70°11.0′	124°49.8′	4.0	124	10
9 May	F1-2	70°11.0′	124°49.8′	3.5	122	NA
13 May	F2-1	69°56.8′	126°10.3′	10.0	170	12
16 May	F2-2	69°56.8′	126°10.3′	1.0	170	15
20 May	F3	71°34.4′	119°36.4′	5.0	132	10
24 May	F4	72°36.6′	126°2.2′	5.0	122	11
28 May	F5	74°30.7′	124°5.9′	3.0	185	14
30 May	D44	71°34.1′	125°17.6′	2.5	85	7
31 May	D45	70°44.5′	124°25.1′	3.0	96	7
2 Jun	F6	70°1.1′	123°45.1′	9.0	163	15
9 Jun	F7-1	69°46.6′	123°37.9′	5.0	134	8
12 Jun	F7-2	69°49.4′	123°38.0′	5.0	115	NA
16 Jun	F8	69°57.4′	125°52.5′	4.0	115	13
18 Jun	F7-3	69°48.9′	123°39.0′	0.0	110	20
21 Jun	FB07	69°58.7′	125°55.4′	5.0	120	15
6 Jul	F9	75°6.4′	120°19.9′	0.0	147	15

[a]NA: Data were not available.

least 18 h in the dark at ~4°C. The supernatant was measured for fluorescence, before and after acidification with 5% HCl, using a Turner Designs fluorometer (model 10-AU) according to the method of *Parsons et al.* [1984]. [Chl *a*] was then calculated using the equation of *Holm-Hansen et al.* [1965] and corrected for filtered seawater dilution. The manufacturer-designated lower detection limit of the fluorometer is 0.025 μg L^{-1}. Analytical variability for 122 duplicate GF/F filters as prepared above was evaluated; the average pairwise difference was 11%, suggesting a standard deviation of the means of 8%.

2.3. DOC and CO

[8] DOC and CO sampling protocols were modified from those of *Xie and Gosselin* [2005]. Briefly, full-length ice cores were cut into 7–9 10 cm thick sections from different depths. The center of each ice section was taken out using a custom-built metal corer (4 cm in diameter, 10 cm in length) and immediately transferred into a 200 mL all-glass syringe (Perfektum®) having been pre-flushed with ambient air and fitted with a three-way nylon gas-tight valve. A known volume of ice plus ambient air was obtained by replacing the syringe's plunger to a pre-set marker. Ambient air was simultaneously collected in duplicate with 10 mL glass syringes (Perfektum®). Both ice and air sampling were performed under conditions that avoided direct sunlight and minimized the influence from the ship's exhaust. Samples were placed in the dark and immediately brought to the nearby ship-based laboratory. After being thawed in a bucket of tap water at room temperature (~20°C), ice samples were gently shaken for 5 min, which was found to be of sufficient duration for attaining gas-liquid equilibrium. The equilibrated headspace gas was transferred into a 5-mL glass syringe and analyzed for [CO] using a Reduction Gas Analyzer (RGA 3) [*Xie et al.*, 2002]. Air samples were analyzed by directly injecting the samples into the analyzer. [CO], reported here as per unit volume of meltwater, was calculated by correcting for [CO] in the ambient air. The lower detection limit was ca. 1 parts per billion by volume (ppbv) for air samples and better than 0.02 nmol L^{-1} for aqueous samples [*Xie et al.*, 2002]. An estimate of analytical variability was made based on 138 duplicate injections of equilibrated headspace gas prepared from in situ ice samples. The average pairwise difference was 3%, suggesting a standard deviation of the means of 2%.

[9] Immediately after the headspace gas transfer for [CO] measurement, the ice meltwater remaining in the 200 mL glass syringes was passed through 0.2 μm polyethersulfone membrane syringe filters (Whatman) and collected into 60 mL glass bottles (Qorpak®). The samples were transported under refrigeration and darkness to the land-based laboratory in Rimouski for determination of DOC concentration ([DOC]). Prior to use, the syringe filters had been profusely rinsed with Nanopure water and the storage glass bottles were soaked with 10% HCl overnight and then thoroughly washed with Nanopure water. Control tests proved the filters and bottles to be free of DOC contamination. DOC samples were acidified to pH ~2 with 25% H_3PO_4 to remove the dissolved inorganic carbon and analyzed in triplicate using a Shimadzu TOC-5000A Total Carbon Analyzer calibrated with potassium biphthalate. The system was checked, at intervals of seven consecutive sample analyses, against Hansell's low-carbon ([DOC]: 1–2 μmol L^{-1}) and deep Sargasso Sea ([DOC]: 44–46 μmol L^{-1}) reference waters. The mean

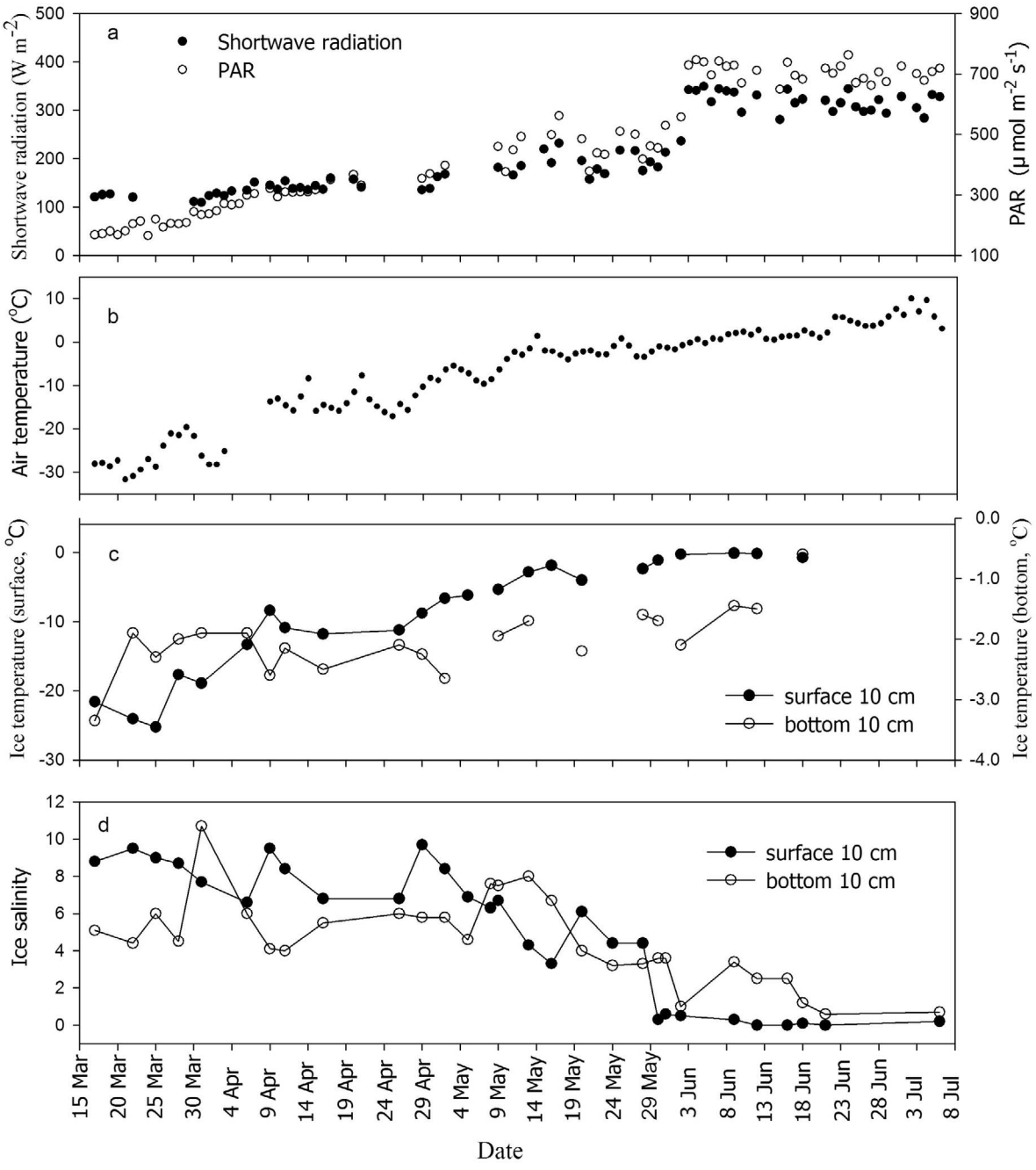

Figure 2. Spatiotemporal variations of (a) daily averaged shortwave, and photosynthetic active radiation (PAR), (b) daily averaged air temperature, (c) sea ice temperature, and (d) bulk sea ice salinity from 17 March to 6 July 2008. See Table 1 for sampling stations corresponding to each sampling date.

coefficient of variation of triplicate measurements was 4% (range: 0.2–13%).

3. Results

3.1. General Meteorological and Hydrological Properties

[10] Over the sampling period, snow depth, ice thickness and ice freeboard ranged from 0 to 10 cm (mean: 4 cm), 72–185 cm (mean: 134 cm) and 6–20 cm (mean: 12 cm), respectively (Table 1). Daily averaged incident shortwave radiation, PAR, and air temperature increased from ca. 160 to 330 W m^{-2}, from ca. 300 to 700 μmol photons m^{-2} s^{-1}, and from ca. −25 to 7°C, respectively (Figures 2a and 2b). Sea ice temperature increased from −21.6 to −0.8°C in the top 10 cm and from −3.4 to −0.6°C in the bottom 10 cm, whereas bulk ice salinity in the corresponding layers decreased from 8.8 to 0.20 and 5.1 to 0.70 (Figures 2c and 2d). From 13 May onward, sea ice started melting and salinity approached zero at certain stations in both the top

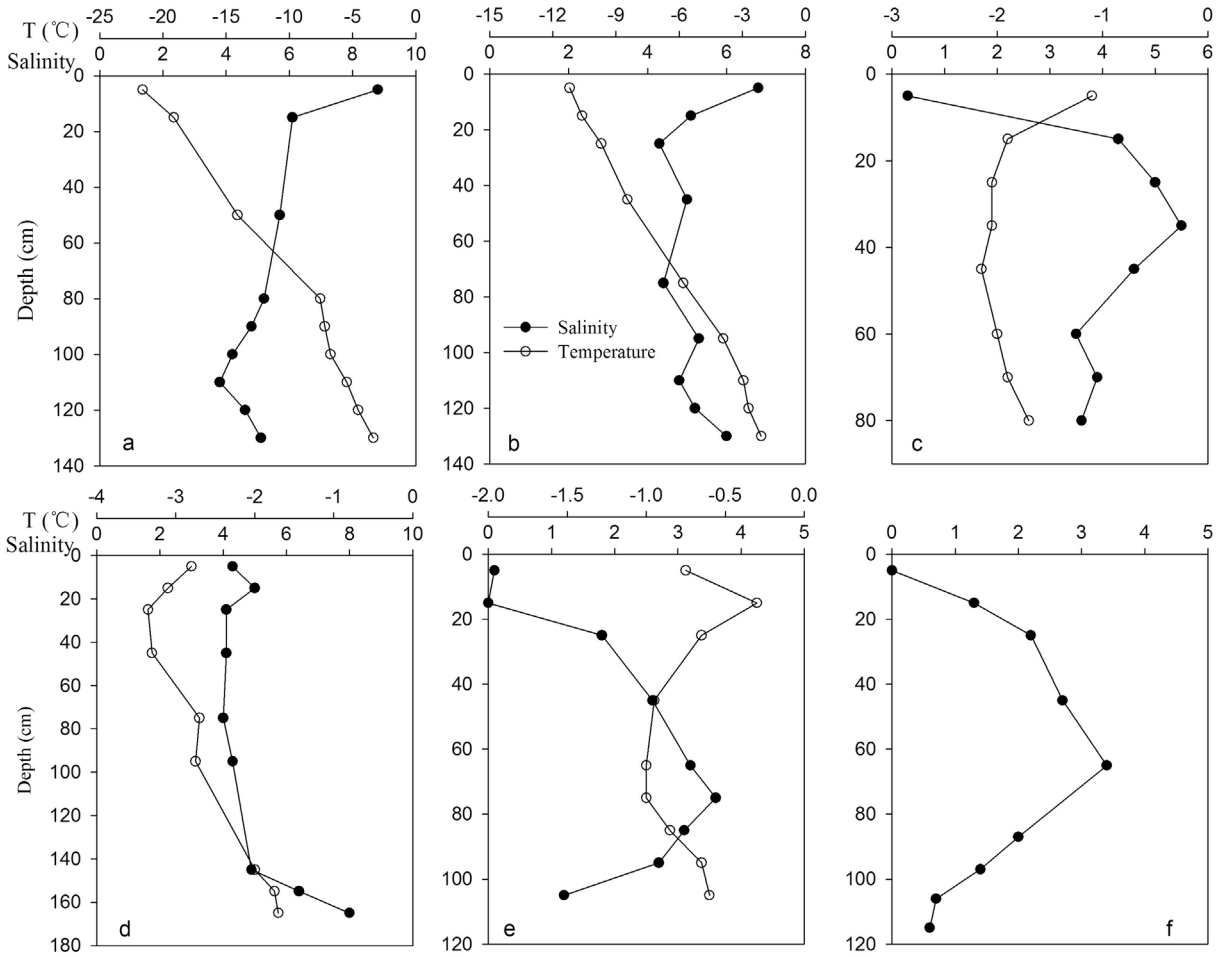

Figure 3. Depth profiles of sea ice salinity and temperature: (a) D29 (17 March, LCP1), (b) D43–1 (26 April, HCP1), (c) D44 (30 May, LCP2), (d) F2 (13 May, HCP2), (e) F7 (18 June, LCP2), (f) FB07 (21 June, LCP2). Temperature data were not available for Stn FB07. Keys: LCP1 = low Chl *a* phase 1; LCP2 = low Chl *a* phase 2; HCP1 = high Chl *a* phase 1; HCP2 = high Chl *a* phase 2. See definitions of these keys in the text.

and bottom layers (Figure 2d) due apparently to nearly complete loss of brine. Imposed over the general trends of these variables were substantial fluctuations resulting from both temporal variation and spatial heterogeneity.

[11] The temporal progression in sea ice temperature profiles was typical for the spring season. Temperature generally increased with depth prior to the start of the melting season (Figures 3a and 2b); after the melting set in, temperature at the surface began to climb and a C-shaped structure formed (Figures 3c and 3e). C-shaped profiles dominated the ice salinity structure before substantial ice melt had occurred (Figures 3a, 3b, and 3d). Once ice melt commenced, bulk ice salinity rapidly decreased at the surface and bottom (Figures 3c, 3e, and 3f). These profiles were consistent with results from previous studies [*Eicken*, 2003; *Toyota et al.*, 2007; *Ehn et al.*, 2011].

3.2. Chlorophyll *a*, DOC, and CO in Surface and Bottom Sea Ice

[12] [Chl *a*] in the surface sea ice layer remained low (<1.0 μg L^{-1}) over the entire sampling period except for two sharp peaks observed in landfast ice near the end of the study (Figure 4a). In the lowermost 10 cm layer, [Chl *a*] gradually increased, peaked twice, and then rapidly decreased to relatively low values for the rest of the study. Based on the variability of [Chl *a*] in bottom ice, the data was grouped into the following periods: low Chl *a* phase 1 (LCP1, 17–31 March), high Chl *a* phase 1 (HCP1, 6 April–5 May), high Chl *a* phase 2 (HCP2, 8–16 May), and low Chl *a* phase 2 (LCP2, 20 May–6 July). LCP1 was sampled exclusively on drifting ice and corresponded to the early stage of ice algal accumulation. HCP1 and HCP2 covered the peak bloom in drifting sea ice and the peak to post-bloom in landfast sea ice, respectively [*Brown et al.*, 2010]. LCP2 was mainly sampled on landfast sea ice (except Stn D44, 30 May) and matched the period of sea ice melt. The overall range of [Chl *a*] in the bottom layer was 1.1 (24 May, Stn F4) to 1570 μg L^{-1} (13 May, Stn F2) with the average concentration for the two high Chl *a* phases (HCPs = HCP1 + HCP2; 561 μg L^{-1}) ~20 times that for the two low Chl *a* phases (LCPs = LCP1 + LCP2; 27 μg L^{-1}). In the bottom layer of drifting ice, mean [Chl *a*] (±s.d.) was 54 ± 43 μg L^{-1} for LCP1 and 310 ± 144 μg

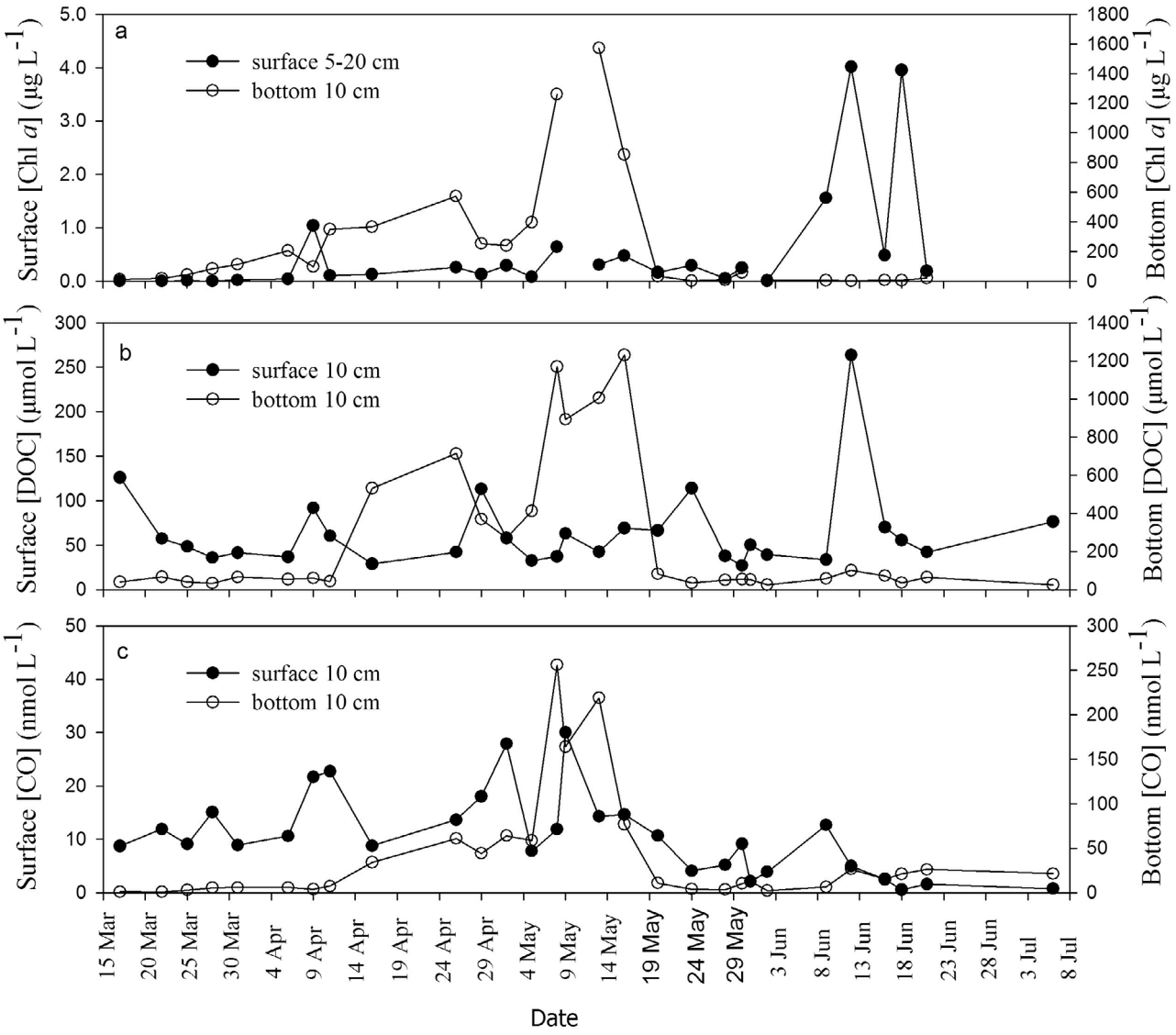

Figure 4. Spatiotemporal variations of (a) chlorophyll *a* (Chl *a*), (b) dissolved organic carbon (DOC), and (c) carbon monoxide (CO) concentrations in surface and bottom sea ice layers from 17 March to 6 July 2008. See Table 1 for sampling stations corresponding to each sampling date.

L^{-1} for HCP1. The only drifting ice station sampled in LCP2, Stn D44, showed that [Chl *a*] dropped to 58 μg L^{-1} during the melting season. In the bottom layer of landfast ice, mean [Chl *a*] was 1230 ± 360 μg L^{-1} for HCP2 and 9 ± 10 μg L^{-1} for LCP2. The mean bottom ice [Chl *a*] of landfast ice was approximately 4 times that of drifting ice for the high Chl *a* phase (HCP).

[13] The general trend of [DOC] at the surface differed from that of [Chl *a*] (Figures 4a and 4b). [DOC] often displayed small but significant variations, even at the same sites sampled over extended periods (e.g., Stn D43) (Figure 4b). The peak at Stn F7 on 12 June (264 μmol L^{-1}) was the dominant feature at the surface. Bottom ice [DOC] was high during the HCPs and low during the LCPs, generally following that of the [Chl *a*]. An exception occurred at the early sampling stage (17 March–11 April) when [DOC] remained low and fairly constant despite a gradual increase

Table 2. Results of Linear Least Squares Regression Analysis Between DOC, CO and Chl *a* in the Bottom 10-cm Sea Ice Layer[a]

Chl *a* phase	R^2	*p*	n
	DOC-Chl a		
LCPs	0.036	0.95	15
HCPs	0.723	<0.001	11
	CO-Chl a		
LCP1	0.941	<0.01	5
LCP2	0.0002	0.97	10
HCPs	0.846	<0.0001	11
	CO-DOC		
LCPs	0.017	0.16	17
HCPs	0.640	<0.001	12

[a]LCPs = low Chl *a* phases; HCPs = high Chl *a* phases; LCP1 = low Chl *a* phase 1; LCP2 = low Chl *a* phase 2. See definitions of these keys in the text.

in [Chl *a*]. Bottom ice [DOC] was linearly correlated with [Chl *a*] during the HCPs but not during the LCPs (Table 2); surface ice [DOC] showed no significant correlation with [Chl *a*] during the entire sampling period ($p > 0.05$). The highest [DOC] (1230 μmol L^{-1}) occurred at Stn F2 on 16 May in landfast ice (Figure 4b). Mean surface [DOC] in drifting ice varied little between LCP1 (62 ± 37 μmol L^{-1}) and HCP1 (58 ± 30 μmol L^{-1}) but decreased to 39 ± 16 μmol L^{-1} in LCP2. Averaged bottom [DOC] in drifting ice was comparable between LCP1 (49 ± 16 μmol L^{-1}) and LCP2 (53 ± 1.8 μmol L^{-1}), but much lower than that of HCP1 (307 ± 247 μmol L^{-1}). In landfast ice, mean [DOC] at the surface increased from 53 ± 16 μmol L^{-1} in HCP2 to 80 ± 69 μmol L^{-1} in LCP2 while at the bottom it was highly enriched during HCP2 (1070 ± 154 μmol L^{-1}) relative to LCP2 (55 ± 25 μmol L^{-1}). On average, bottom landfast ice contained > 3 times DOC than bottom drifting ice during the HCPs (1070 versus 307 μmol L^{-1}).

[14] [CO] in the upper 10 cm layer ranged from 0.57 to 30.0 nmol L^{-1} (mean: 10.8 ± 8 nmol L^{-1}) (Figure 4c) and was supersaturated relative to the atmosphere (~100 ppbv), consistent with previous findings [*Xie and Gosselin*, 2005]. [CO] fluctuated, often erratically, over the entire sampling period, including those stations that were sampled multiple times (e.g., Stns D33 and D43) (Figure 4c). However, a substantial [CO] drawdown was evident after 13 May, which coincided with the start of ice melt. [CO] distribution at the surface showed no similarity to those of [Chl *a*] and [DOC]. Bottom ice [CO] generally corresponded to [Chl *a*] and [DOC], showing peak concentrations during the HCPs. [CO] at the bottom increased slowly during LCP1, tracking the trend of [Chl *a*]. At the surface of drifting ice, mean [CO] was 10.7 ± 3 nmol L^{-1} for LCP1, 16.4 ± 7 nmol L^{-1} for HCP1, and 5.6 ± 5 nmol L^{-1} for LCP2; mean values at the bottom were 3.2 ± 2, 34.8 ± 26, and 11.5 ± 2 nmol L^{-1} for the corresponding Chl *a* phases. Mean surface [CO] in landfast ice decreased from 17.7 ± 8 nmol L^{-1} in HCP2 to 4.7 ± 4 nmol L^{-1} in LCP2. Similarly, mean bottom [CO] decreased from 179 ± 78 to 13.7 ± 10 nmol L^{-1}. The mean bottom ice [CO] of landfast ice was 5 times that of drifting ice (179 versus 34.8 nmol L^{-1}) during the HCPs. Surface [CO] showed no significant relationship with [Chl *a*] and [DOC] ($p > 0.05$). However, bottom [CO] was linearly correlated with [Chl *a*] during the HCPs and LCP1, but not LCP2 (Table 2). Bottom ice [CO] was also significantly correlated with [DOC] during the HCPs. Partial correlation analysis indicated that this relationship largely stemmed from the correspondence of [DOC] to [Chl *a*] (see above).

3.3. Vertical Distributions of Chl *a*, DOC, and CO

[15] [Chl *a*] profiles in drifting ice were typically L-shaped during both low and high Chl *a* phases (Figures 5a–5c). Profiles in landfast ice were also L-shaped during HCP2 (Figure 5d) but strayed from the L-shape and exhibited multiple peaks during LCP2 (Figures 5e and 5f).

[16] In contrast to [Chl *a*] profiles, [DOC] profiles during LCP1 showed decreasing [DOC] from the surface to the middle sections and less variation at deeper depths (Figure 5a). [DOC] was < 131 μmol L^{-1} throughout the ice column. [DOC] during the HCPs remained low at the surface but was slightly elevated relative to the depths immediately below (Figures 5b and 5d). The extreme DOC enrichment in bottom ice, however, obscured this character, resulting in an overall L-shaped distribution that paralleled that of [Chl *a*] (Figures 5b and 5d). [DOC] in the lowermost 10 cm layer reached > 700 μmol L^{-1} in drifting ice (Figure 5b) and > 1000 μmol L^{-1} in landfast ice (Figure 5d). Note that DOC enrichment started at ~30 cm up from the bottom, but the strongest enrichment was within the lowermost section (Figures 5b and 5d). During the melting season (LCP2), [DOC] vertical structures varied from station to station and often displayed zigzag patterns that were either alike (Figure 5e) or dissimilar (Figure 5c) to that of [Chl *a*]. The marked near-bottom peak at Stn FB07, matching no [Chl *a*] counterpart, was unique among all [DOC] profiles obtained (Figure 5f).

[17] Vertical profiles of [CO] during LCP1 generally mimicked those of [DOC] (Figure 5a). During the HCPs, [CO] was slightly elevated within the surface ice, reached a minimum toward the middle, and increased rapidly at the bottom (Figures 5b and 5d). Depth distributions in the melting season were less regular and variable from station to station. The [CO] profile at Stn D44 followed the [DOC] profile within the upper portion of the ice column but was opposite in the lower portion (Figure 5c). [CO] at Stn F7 was lowest at the surface and moderately high and rather constant in the intermediate layer and then increased at the bottom, dissimilar to the [DOC] and [Chl *a*] profiles (Figure 5e). Stn FB07 was characterized by a sharp [CO] peak near the bottom that paralleled the [DOC] spike and displayed the greatest [CO] (762 nmol L^{-1}) observed in this study (Figure 5f). These unusually high [CO] and [DOC] were excluded from the calculations of depth-integrated and -weighted concentrations of DOC and CO in section 3.4.

3.4. Depth-Integrated and -Weighted Concentrations of Chl *a*, DOC, and CO

[18] Depth-integrated concentrations, also referred to as column burdens (subscript cb), of Chl *a*, DOC, and CO for the entire ice core were obtained by the trapezoid method, assuming homogenous distributions of these variables within the top and bottom ice sections sampled. Depth-weighted concentrations (subscript dw) were derived by dividing column burdens by the total depth of the ice core. Table 3 summarizes the column burdens and depth-weighted concentrations. $[\text{Chl } a]_{cb}$ and $[\text{Chl } a]_{dw}$ ranged from 0.30 to 161 mg m^{-2} (mean: 25 ± 7 mg m^{-2}), and from 0.25 to 103 μg L^{-1} (mean: 18 ± 6 μg L^{-1}), respectively. $[\text{Chl } a]_{cb}$ in the HCP was 4.5 times that in LCP1 for drifting ice and 53 times that in LCP2 for landfast ice. $[\text{Chl } a]_{dw}$ followed a similar trend with slightly different HCP-to-LCP ratios. $[\text{Chl } a]_{cb}$ and $[\text{Chl } a]_{dw}$ in landfast ice for HCP2 were approximately 5 and 4 times higher, respectively, than those in drifting ice for HCP1.

[19] $[\text{DOC}]_{cb}$ and $[\text{DOC}]_{dw}$ spanned from 25 to 251 mmol m^{-2} (mean: 87 ± 51 mmol m^{-2}) and 23 to 148 μmol L^{-1} (mean: 64 ± 33 μmol L^{-1}), respectively. In drifting ice, $[\text{DOC}]_{cb}$ and $[\text{DOC}]_{dw}$ in HCP1 were both ~40% higher than those in the LCPs (Table 3). In landfast ice, $[\text{DOC}]_{cb}$ and $[\text{DOC}]_{dw}$ in HCP2 were both more than twice those in LCP2. As expected, $[\text{DOC}]_{cb}$ and $[\text{DOC}]_{dw}$ in landfast ice were higher compared to those in drifting ice. The cruise-mean $[\text{DOC}]_{cb}$ was 5.3% of the concurrently determined $[\text{DOC}]_{cb}$ in the under-ice surface mixed layer (1.63 ± 0.6 mol

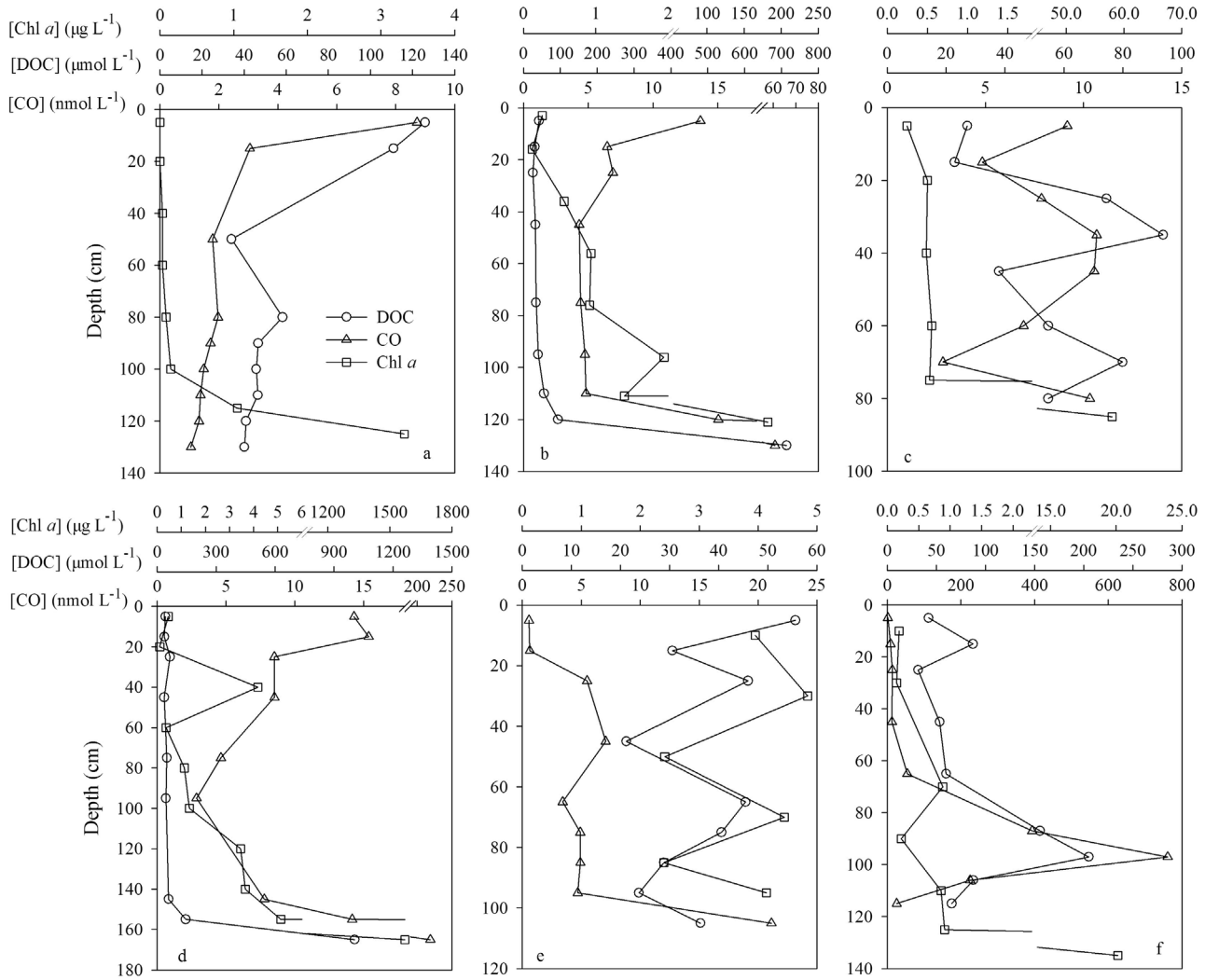

Figure 5. Depth profiles of sea ice chlorophyll *a* (Chl *a*), dissolved organic carbon (DOC) and carbon monoxide (CO) concentrations. (a) D29 (17 March, LCP1), (b) D43–1 (26 April, HCP1), (c) D44 (30 May, LCP2), (d) F2 (13 May, HCP2), (e) F7 (18 June, LCP2), and (f) FB07 (21 June, LCP2). Keys and definitions of LCP1, LCP2, HCP1, and HCP2 are the same as those in Figure 3.

m^{-2}) that was 19 m deep on average (M. Gosselin, unpublished data, 2008).

[20] $[CO]_{cb}$ and $[CO]_{dw}$ ranged from 3.2 to 41.2 μmol m^{-2} (mean: 13.9 ± 10 μmol m^{-2}) and 2.0 to 33.2 nmol L^{-1} (mean: 10.6 ± 8 nmol L^{-1}), respectively. In drifting ice, both $[CO]_{cb}$ and $[CO]_{dw}$ in HCP1 were about twice those in LCP1 but the differences between HCP1 and LCP2 were smaller (Table 3). In landfast ice, $[CO]_{cb}$ and $[CO]_{dw}$ in

Table 3. Comparison of Depth-Integrated (i.e., Column Burden) and Depth-Weighted Concentrations of Chl *a*, DOC, and CO Between Drifting and Landfast Sea Ice and Among Different Chl *a* Phases[a]

	Drifting Ice			Landfast Ice	
	LCP1	HCP1	LCP2[b]	HCP2	LCP2[c]
$[Chl\ a]_{cb}$ (mg m^{-2})	1.4–12 (5.7 ± 4)	10–44 (26 ± 13)	6.2	(87–161) (126 ± 37)	(0.30–4.3) (2.4 ± 2)
$[Chl\ a]_{dw}$ (μg L^{-1})	1.1–8.2 (4.0 ± 3)	9.4–23 (21 ± 9)	6.9	50–103 (82 ± 28)	0.25–3.8 (1.9 ± 1)
$[DOC]_{cb}$ (mmol m^{-2})	39–93 (62 ± 24)	39–122 (78 ± 26)	25–47 (36 ± 15)	152–251 (188 ± 45)	38–113 (74 ± 26)
$[DOC]_{dw}$ (μmol L^{-1})	26–62 (43 ± 17)	43–91 (60 ± 16)	26–55 (41 ± 21)	110–148 (128 ± 15)	23–97 (57 ± 23)
$[CO]_{cb}$ (μmol m^{-2})	3.2–12.6 (5.7 ± 4)	5.5–19.0 (11.3 ± 4)	6.8–7.9 (7.3 ± 0.8)	24.0–41.2 (33.4 ± 7)	3.3–26.2 (13.4 ± 7)
$[CO]_{dw}$ (nmol L^{-1})	2.4–8.4 (3.9 ± 3)	4.3–13.5 (8.7 ± 3)	7.9–8.3 (8.1 ± 0.2)	14.1–33.2 (23.8 ± 8)	2.0–21.5 (10.5 ± 6)

[a]Subscript "cb" designates column burden and "dw" designates depth-weighted concentrations. Values are range and, in parentheses, mean ± s.d. Keys and definitions of LCP1, LCP2, HCP1, and HCP2 are the same as those in Figure 3.
[b][Chl *a*] data were collected only at Stn D44 on 30 May 2008.
[c]Stn FB07 is excluded for calculations of $[DOC]_{cb}$, $[DOC]_{dw}$, $[CO]_{cb}$, and $[CO]_{dw}$.

HCP2 were 2.5 times greater than those in LCP2. $[CO]_{cb}$ and $[CO]_{dw}$ in landfast ice were about twice those in drifting ice.

4. Discussion

4.1. Comparison With Previous Studies

[21] Published studies on DOC distributions in first-year sea ice are rare and exclusively focused on the lowermost 4 cm of landfast ice [*Smith et al.*, 1997; *Riedel et al.*, 2008]. Our finding of co-variation between [DOC] and [Chl *a*] in the bottom layer is consistent with the previous studies. Our peak-bloom (HCP2) DOC concentrations ([DOC]s) in the bottom layer of the landfast sea ice in the western Canadian Arctic (893–1230 μmol L^{-1}) were lower than those in the Resolute area, eastern Canadian Arctic under thin snow cover (1000–3358 μmol L^{-1}) [*Smith et al.*, 1997]. This could be due partly to the higher ice algal biomass observed in the Resolute area ([Chl *a*]: 700–2480 μg L^{-1}) than in the present study ([Chl *a*]: 854–1260 μg L^{-1}). Furthermore, our thicker ice sampling layer (10 versus 4 cm) should also substantially contributed to this difference, given that ice algae and DOC are enriched predominantly within the very thin bottom layer. *Riedel et al.* [2008] reported a mean [DOC] of ~800 μmol L^{-1} in the bottom 4 cm of landfast sea ice in Franklin Bay, western Canadian Arctic under thin snow cover during the vernal ice algal bloom season. Corresponding mean [DOC] from our study, 1070 μmol L^{-1}, was higher even without taking into account the difference in the ice sampling thickness, in accordance with more abundant Chl *a* observed in the present study (854–1260 versus < 872 μg L^{-1}).

[22] Vertical CO profiles collected during the HCPs resembled those previously documented in Franklin Bay [*Xie and Gosselin*, 2005]. However, in the present study, we observed a substantially higher mean [CO] in the bottom 10 cm layer (179 nmol L^{-1}) than the earlier study (81.4 nmol L^{-1} in the bottom 4 cm layer). Accordingly, the mean $[CO]_{dw}$ and $[CO]_{cb}$ from the present study, 23.8 nmol L^{-1} and 33.6 μmol m^{-2}, are greater than the values of 15.3 nmol L^{-1} and 29.4 μmol m^{-2} reported by *Xie and Gosselin* [2005]. The smaller difference in $[CO]_{cb}$ is due to thicker sea ice during the previous survey (mean ice thickness: 134 versus 192 cm). The cruise-mean $[CO]_{cb}$ in sea ice is approximately 3 times and 21% of the CO inventories observed in the open water of the Amundsen Gulf in fall 2003 and late spring 2004, respectively [*Xie et al.*, 2009a].

4.2. Factors Controlling [DOC] and [CO] in Sea Ice

[23] Significant relationships between [DOC] and [Chl *a*] (Table 2) suggested that primary production was the main control on DOC accumulation in bottom sea ice during the HCPs, in accordance with previous studies [*Smith et al.*, 1997; *Riedel et al.*, 2008], but not within the upper ice matrix and during the LCPs. Other processes influencing DOC distribution in sea ice include trapping of riverine and resuspended organic matter during ice formation [*Rachold et al.*, 2004], aeolian organic matter deposition, chemical enrichment in the quasi-liquid layer at the surface [*Grannas et al.*, 2007], brine drainage [*Giannelli et al.*, 2001; *Amon*, 2004], and microbial [*Amon et al.*, 2001] and photochemical remineralization [*Belzile et al.*, 2000; *Xie and Gosselin*, 2005]. Inclusion of resuspended or riverine organic matter into ice could be attributable to the marked near-bottom [DOC] peak observed at Stn FB07 (Figure 5f). Similar CDOM peaks have been observed in Franklin Bay [*Xie and Gosselin*, 2005]. Atmospheric deposition and organic matter accumulation in the quasi-liquid layer might be responsible for the frequent DOC enrichment at the surface (Figures 5a and 5e). Brine drainage most likely resulted in the rapid [DOC] drawdown in bottom ice at the onset of ice melting (Figures 4b, 5c, 5e, and 5f). To further elucidate this point, we calculated brine volume fractions (B_f) according to *Cox and Weeks* [1983] and assumed that significant fluid transport occurs in first year sea ice at $B_f \geq 5\%$ [*Golden et al.*, 1998]. B_f in the top 10 cm increased by ca. 4 times from the pre-melting (before 13 May; 4.4% ± 2%) to the melting season (after 13 May; 16% ± 7%). Similarly, B_f within the interior ice increased by ca. 3 times from 4.4% (±3%) to 13% (±6%) over the same period of time. B_f in the bottom 10 cm ranged from 7.2% to 32% and on average was only moderately higher during the melting season (18% ± 8%) than during the preceding period (14% ± 7%). Bottom ice was thus permeable to fluids over the entire sampling period while surface and interior ice were permeable only during the period of ice melt. Brine drainage, which requires compensation by melting in the upper layers [*Tison et al.*, 2008], should thus take place primarily during the melting season when the entire ice column was fluid-permeable.

[24] Notably, exchange of interior ice brine with the atmosphere and ocean can be impeded by the formation of superimposed ice as fresh ice melt comes in contact with interior ice temperature below its freezing temperature near the surface and bottom of the ice cover [*Eicken*, 1992; *Ehn et al.*, 2011]. This process has been suggested to be responsible for the development of a distinct interior ice community during advanced stages of ice melt [*Mundy et al.*, 2011]. This formation of superimposed ice contributes to the explanation of why vertical distributions of [DOC] during the melting season were more erratic than during the previous periods, particularly within the interior ice (Figures 5c and 5e).

[25] The significant relationships between [CO] and [Chl *a*] suggest that [CO] distribution in the bottom ice prior to the melting season was dictated by biological processes and chemical reactions involving algal particles and algae-derived DOM. Based on controlled laboratory experiments and field observations, *Xie and Gosselin* [2005] proposed that CO photoproduction from CDOM is the principal driving force creating the distinct sea-ice [CO] vertical structure during the ice algal bloom season: lowest near the middle, highly elevated at the bottom, and moderately enriched at the surface (Figures 5b and 5d). Solar-simulated irradiations of sea ice and brine samples collected from the IPY-CFL project further confirmed the CDOM photochemical source (H. Xie, unpublished data, 2008). Moreover, *Xie and Zafiriou* [2009] discovered that photodegradation of particulate organic matter (POM) in seawater is also an important CO production pathway. A later study further suggests that marine POM is more efficient than marine CDOM at CO photoproduction, particularly at visible wavelengths (G. Song and H. Xie, unpublished data, 2009). As relatively more visible radiation reaches the bottom ice due to stronger reflection of UV radiation by snow and ice [*Wiscombe and Warren*, 1980; *Winther et al.*, 2004], this evidence is of great significance to

the high Chl *a* phases when POM can be more abundant than DOM in the bottom ice [*Smith et al.*, 1997; *Riedel et al.*, 2008]. Additionally, prolific oxygen production due to photosynthesis by ice algae [*Gleitz et al.*, 1995; *Delille et al.*, 2007] promotes CO photoproduction since high oxygen concentrations accelerate organic matter photooxidation [*Gao and Zepp*, 1998; *Xie et al.*, 2004]. If CDOM and POM photochemistry were the primary CO sources, then the pre-HCP [CO] in sea ice should decrease with depth as a consequence of progressive light attenuation through ice and of weak organic matter enrichment at the bottom, as was observed in the pre-HCP vertical CO profiles (Figure 5a).

[26] Besides photochemistry, organic matter thermal (dark) reactions also produce CO with its formation rate rising quickly above pH 8 [*Zhang et al.*, 2008]. Although low temperatures in sea ice are not favorable for dark CO production, the highly elevated levels of organic matter and pH (up to 10) [*Gleitz et al.*, 1995] associated with the ice algal bloom suggest that this process can be potentially important to bottom ice CO production. Moreover, *Gros et al.* [2009] observed significant CO production in laboratory cultures of marine phytoplankton, particularly certain diatoms. The strong correlation between [CO] and [Chl *a*] found in the present study during the early stage of the ice algal accumulation (LCP1) offers circumstantial field evidence for this argument. Further investigations, particularly laboratory incubations, are needed to elucidate whether ice algae, among which diatoms often dominate in the Arctic first-year sea ice [*Horner*, 1985; *Riedel et al.*, 2008; *Różańska et al.*, 2009], are important CO producers.

[27] The nature of multiple formation pathways implies that CO production in sea ice commenced during freeze up around mid-October of the preceding year and sustained all the way toward the end of the melting season in summer. The strength and mechanism of CO production, however, varied in response primarily to the seasonal periodicity of solar radiation. The production is expected to be moderate and mainly CDOM photochemistry-based in fall, minimal and virtually exclusively thermal reaction-induced in winter, and maximal and largely photochemically and biologically driven in spring and summer. The continued increase in [CO] in the middle layer during the melting season (data not shown), where CO loss was weaker than at the upper and lower interfaces (see below), was indicative of continued CO production after the disappearance of the high ice algal biomass. Vanishing snow cover and thawing surface sea ice in the melting season allow more UV radiation to enter the ice, thereby facilitating CO photoproduction.

[28] Loss of CO in sea ice results from microbial uptake, upward release into the atmosphere, and downward transport into the water column. Microbial CO uptake, though well-documented in various marine water bodies [*Conrad et al.*, 1982; *Tolli and Taylor*, 2005; *Xie et al.*, 2005, 2009a, 2009b], has been little studied in sea ice. Limited published data suggests that this process in sea ice is relatively slow but significant with turnover times from ~10 d in the high-biomass bottom layer to several tens of days in the much less biologically active upper layer [*Xie and Gosselin*, 2005]. Surface ice temperature was close to or above −10°C from 6 April onward (Figure 2c), suggesting that the ice matrix was diffusive to gas transport [*Gosink et al.*, 1976; *Loose et al.*, 2009, 2011]. The supersaturated state of CO (see section 3.2) hence led to an egress of this gas from ice to the atmosphere. Warmer surface ice temperatures during the melting season (range: −0.1 to −4°C; mean: −1.5°C) greatly enhanced gas diffusion and brine movement (see above), thereby boosting ice-to-air gas exchange and lowering [CO] within the surface layer (Figure 4c). Similar to DOC, the abrupt loss of CO at the start of ice melt in the bottom ice (Figure 4c) most likely resulted from brine drainage and the irregularity of [CO] vertical distributions during the melting season, particularly within the interior ice (Figures 5c and 5e), was plausibly linked to the formation of superimposed ice.

4.3. Net Production of DOC and CO

[29] Biological DOC production in the ice took place predominantly during the HCPs and within the lowermost 30-cm layer (see sections 3.2 and 3.3). Depth-integrated [DOC] in that layer averaged over the HCP was 127 ± 22 mmol m^{-2} in landfast ice and 57 ± 19 mmol m^{-2} in drifting ice excluding data from 6 to 11 April when [DOC] remained low (Figure 4b). Net biological DOC production was estimated as the difference between [DOC] in the HCP and that in LCP1, taking the mean depth-integrated [DOC] in the lowermost 30-cm layer for LCP1 (13 ± 5 mmol m^{-2}) as the background [DOC]. This gave a net DOC production of 114 ± 22 mmol m^{-2} in landfast ice and 44 ± 19 mmol m^{-2} in drifting ice. The net biological DOC production averaged for both the landfast and drifting ice (75 ± 29 mmol m^{-2} or 1.9 ± 0.7 mmol m^{-2} d^{-1} over a period of 40 d) is comparable to the ice algal DOC release rate in the Chukchi Sea (1.6 ± 2 mmol m^{-2} d^{-1}) estimated by *Gosselin et al.* [1997] using deck incubations. Our value is also similar in magnitude to the annual ice algal primary production (~80 mmol m^{-2} a^{-1}) modeled by *Lavoie et al.* [2009] for the Mackenzie Shelf and corresponds to 45–90% of the spring primary production of ice algae on the shelves of the Chukchi and Beaufort Seas (83–167 mmol m^{-2}) [*Gradinger*, 2009]. The majority of this newly produced DOC would be released into the water column during the melting season as inferred from the precipitous [DOC] drop at the onset of bottom ice melt in mid-May (Figure 4b). Notably, the net DOC production estimated here omits any biological DOC formation occurring during the melting season and does not take into account DOC loss processes as elaborated above. Therefore, our estimate is believed to be conservative and thus underestimates the gross DOC production. In contrast, all our ice cores were taken under relatively low snow covers (≤10 cm), which reportedly favor biological DOC production over higher snow covers [*Riedel et al.*, 2008]. This potentially leads to upward biases in our estimates. However, we note that snow depths of greater than 15 cm were not common during the present study, except near deformed ice (C. J. Mundy, unpublished data, 2008) and that maximum Chl *a* concentrations during HCP2 were observed under a medium snow cover (10–15 cm), reaching > 3000 μg L^{-1} (M. Gosselin, unpublished data, 2008).

[30] Net production of CO in the bottom 30-cm layer during the HCPs, assessed with an approach similar to that for DOC, was 6.5 ± 2 μmol m^{-2} in drifting ice, 21.5 ± 9 μmol m^{-2} in landfast ice, and 13.2 ± 9 μmol m^{-2} averaged for the two. For comparison, the parallel CO net production in the whole ice column was 7.2, 27.5, and 15.3 μmol m^{-2}, respectively, demonstrating that CO production primarily

took place within the bottom layer. Furthermore, we estimated the CO net production from the start of ice formation to the end of the HCPs as 11.3 μmol m^{-2} in drifting ice, 33.4 μmol m^{-2} in landfast ice, and 18.7 μmol m^{-2} averaged for the two, assuming negligible inclusion of CO from seawater during ice formation [*Xie and Gosselin*, 2005]. These estimates are only moderately higher than those for the HCPs due apparently to low CO production over the extended dark winter period. It is again noted that all above estimates were lower limits of the corresponding gross production rates since various loss processes were not taken into account.

4.4. Contribution of Sea Ice to Atmospheric CO

[31] As sea ice in our study area was supersaturated with CO, it acted as a source of CO to the atmosphere. Only the Amundsen Gulf was evaluated with regard to the CO flux to the atmosphere since the majority of the sampling stations were located in this region (Figure 1). The CO flux can be roughly estimated by multiplying a sea-ice CO transfer velocity of 0.70 m d^{-1} [*Xie and Gosselin*, 2005] by the cruise-mean surface ice [CO] (11.7 ± 8 nmol L^{-1}) in the Amundsen Gulf. Here the sea-ice CO transfer velocity is based on the study by *Fanning and Torres* [1991] indicating that ice cover reduces the ^{222}Rn transfer velocity by ~80%. The resultant ice-to-air flux estimate was 8.2 ± 5 μmol m^{-2} d^{-1}, which is 45% of the CO flux from the open seawater to the atmosphere in the Amundsen Gulf in spring 2004 [*Xie et al.*, 2009a]. This value translates to an annual area-integrated flux of 7.4 × 10^7 moles of CO in the Amundsen Gulf by applying it to the period from mid-March to mid-July and taking a mean sea ice area of 7.4 × 10^4 km^2 (Canadian Ice Service, 2009, http://ice-glaces.ec.gc.ca/IceGraph103/page1.jsf). Therefore, the annual sea ice CO flux is > 74% of that from the open water in the same region [*Xie et al.*, 2009a]. Note that the flux estimates made here omit the period from the start of ice formation (mid-October 2007) to mid-March 2008 over which sea ice [CO] is unknown. This underestimates the annual flux, though fluxes during wintertime are likely low due to low CO production and low ice permeability. It must be mentioned that there could be potentially large uncertainties in our CO flux estimates associated with using a constant transfer velocity. Unlike air-sea gas exchange, which has been relatively well parameterized by wind speed [e.g., *Wanninkhof*, 1992], there are currently no acceptable parameterizations for air-sea ice gas exchange. Gas transfer through sea ice should be dominated by diffusive processes controlled by the porosity of sea ice [*Gosink et al.*, 1976; *Loose et al.*, 2011]. As porosity is a function of sea ice temperature [*Cox and Weeks*, 1983], gas permeability is expected to change seasonally. A recent laboratory simulation study, conducted at ice surface temperatures of −4 to −12°C, observed significant gas diffusion but was unable to find a consistent relationship between gas diffusion and sea ice porosity within the porosity range encountered (0.061–0.079) [*Loose et al.*, 2011]. Therefore, our CO flux estimates represent a first-approximation and will likely need to be refined upon the advent of a quantitative understanding of gas transfer across the air-sea ice interface.

[32] In addition to the direct emission of CO from ice, part of the CO released from ice into the water column is also exchanged to the atmosphere when the ice cover breaks up or through leads and polynyas. $[CO]_{cb}$ lacked a consistent drawdown during LCP2 (data not shown), implying that CO production during that time was no less than losses caused by melting, brine drainage, microbial uptake, and emission to air. The sea-ice CO stock in LCP2 (12.3 ± 7 μmol m^{-2}) can, therefore, be considered the lower limit transferred to and trapped in surface seawater through melting. According to *Xie et al.* [2009a], microbial uptake and outgassing each accounts for half of the CO loss in the mixed layer of the Amundsen Gulf in spring. Consequently, 50% of the sea-ice CO released to the surface seawater ended up in the atmosphere, i.e., 6.2 μmol m^{-2} or 3.5 × 10^5 moles of CO, taking the mean sea ice area of 5.7 × 10^4 km^2 during LCP2 (Canadian Ice Service, 2009, http://ice-glaces.ec.gc.ca/IceGraph103/page1.jsf). This represents only 0.5% of the direct ice-to-air flux assessed above.

5. Summary and Conclusions

[33] [DOC] and [CO] in the bottom sea ice generally followed the progression of ice algal biomass (as inferred by [Chl *a*]) while no consistent trends existed at the surface. Both [DOC] and [CO] decreased from the surface to the bottom of the ice at the start of the study during the period of low sea ice [Chl *a*]. During the peak ice algal bloom, [DOC] and [CO] decreased toward the interior of the ice cover and were highly enriched at the bottom. During the period of ice melt, the vertical structure of [CO] usually differed from that of [DOC] and both displayed no consistent patterns. It is noteworthy that bottom landfast ice in the study area contained higher concentrations of DOC and CO than bottom drifting ice during the period of high ice algal biomass.

[34] Biological production during the peak period of the ice algal bloom and brine drainage-linked loss in the melting season were the dominant factors controlling the evolution of [DOC] in the bottom sea ice. The spatiotemporal distributions of [CO] in sea ice was in accordance with an in situ CO production by photooxidation of both dissolved and particulate organic matter, though the possibility of direct biological CO production, particularly during the peak period of the ice algal bloom, could not be ruled out. CO loss appeared fastest in the melting season as rising temperatures accelerated brine drainage, microbial consumption, and outgassing.

[35] While DOC stock in sea ice was much smaller than its counterpart in the underlying water column surface mixed layer, CO inventories in sea ice and sunlit ice-free waters were of the same magnitude. Biological DOC production constituted a significant part of the ice algal primary production. Net accumulations of both DOC and CO predominantly occurred within the bottom ice layer when ice algal biomass was at its maximum. It is suggested that sea ice is an important source of atmospheric CO with its source strength approaching that of the ice-free water in spring. If this preliminary evaluation of CO flux is confirmed in the future, then Arctic climate warming, which leads to a shrinking ice cover, is not expected to substantially increase the CO flux to the atmosphere in spite of anticipated increases in the ice-free water area and water column CO production.

[36] **Acknowledgments.** We thank C. Nozais, S. Pineault, C. Lacoste, J. Ehn, R. Memorana, and many other colleagues for their help with sea ice coring; G. Carnat, J. Ehn, and others for sea ice temperature measurement; M. Simard for DOC analysis; and D. A. Hansell and W. Chen for providing the DOC certified reference materials. We appreciate the cooperation of the chief scientists, captains, and crews of the Circumpolar Flaw Lead (CFL) system study cruises. This study was supported by grants from the Canadian International Polar Year (IPY) federal program office and the Natural Sciences and Engineering Research Council of Canada (NSERC). G.S. and Y.Z. were supported by graduate scholarships from HX's NSERC Discovery Grant, CFL, and the Institut des sciences de la mer de Rimouski (ISMER). C.A. was supported by funds from CFL and the IPY Arctic Surface Ocean–Lower Atmosphere Study (Arctic SOLAS) program. C.J. M. was supported by a postdoctoral fellowship from the Fonds québécois de la recherche sur la nature et les technologies (FQRNT). The CFL and Arctic SOLAS programs are under the overall directions of D. Barber and M. Levasseur, respectively. This is a contribution to the research programs of CFL, Arctic SOLAS, ISMER, and Québec-Océan.

References

Amon, R. M. W. (2004), The role of dissolved organic matter for the organic carbon cycle in the Arctic Ocean, in *The Organic Carbon Cycle in the Arctic Ocean*, edited by R. Stein and R. W. Macdonald, pp. 83–99, doi:10.1007/978-3-642-18912-8_4, Springer, New York.

Amon, R. M. W., H.-P. Fitznar, and R. Benner (2001), Linkages among the bioreactivity, chemical composition, and diagenetic state of marine dissolved organic matter, *Limnol. Oceanogr.*, *46*(2), 287–297, doi:10.4319/lo.2001.46.2.0287.

Barber, D. G., M. Asplin, Y. Gratton, J. Lukovich, R. Galley, R. Raddatz, and D. Leitch (2010), The international polar year (IPY) circumpolar flaw lead (CFL) system study: Introduction and physical system, *Atmos. Ocean*, 225–243.

Bates, T. S., K. C. Kelly, J. E. Johnson, and R. H. Gammon (1995), Regional and seasonal variations in the flux of oceanic monoxide to the atmosphere, *J. Geophys. Res.*, *100*(D11), 23,093–23,101, doi:10.1029/95JD02737.

Belzile, C., S. C. Johannessen, M. Gosselin, S. Demers, and W. L. Miller (2000), Ultraviolet attenuation by dissolved and particulate constituents of first-year ice during late spring in an Arctic polynya, *Limnol. Oceanogr.*, *45*(6), 1265–1273, doi:10.4319/lo.2000.45.6.1265.

Belzile, C., J. A. E. Gibson, and W. F. Vincent (2002), Colored dissolved organic matter and dissolved organic carbon exclusion from lake ice: Implications for irradiance transmission and carbon cycling, *Limnol. Oceanogr.*, *47*(5), 1283–1293, doi:10.4319/lo.2002.47.5.1283.

Brown, T. A., S. T. Belt, B. Philippe, C. J. Mundy, G. Massé, M. Poulin, and M. Gosselin (2010), Temporal and vertical variations of lipid biomarkers during a bottom ice diatom bloom in the Canadian Beaufort Sea: Further evidence for the use of the IP_{25} biomarker as a proxy for spring Arctic sea ice, *Polar Biol.*, doi:10.1007/s00300-010-0942-5, in press.

Bunch, J. N., and R. C. Harland (1990), Bacterial production in the bottom surface of sea ice in the Canadian subarctic, *Can. J. Fish. Aquat. Sci.*, *47*(10), 1986–1995, doi:10.1139/f90-223.

Conrad, R., W. Seiler, G. Bunse, and H. Giehl (1982), Carbon monoxide in seawater (Atlantic Ocean), *J. Geophys. Res.*, *87*(C11), 8839–8852, doi:10.1029/JC087iC11p08839.

Cox, G. F. N., and W. F. Weeks (1983), Equations for determining the gas and brine volumes in sea-ice samples, *J. Glaciol.*, *29*, 306–316.

Delille, B., B. Jourdain, A. V. Borges, J.-L. Tison, and D. Delille (2007), Biogas (CO_2, O_2, dimethylsulfide) dynamics in spring Antarctic fast ice, *Limnol. Oceanogr.*, *52*(4), 1367–1379, doi:10.4319/lo.2007.52.4.1367.

Doney, S. C., R. G. Najjar, and S. Stewart (1995), Photochemistry, mixing and diurnal cycles in the upper ocean, *J. Mar. Res.*, *53*, 341–369, doi:10.1357/0022240953213133.

Ehn, J. K., C. J. Mundy, D. G. Barber, H. Hop, A. Rossnagel, and J. Stewart (2011), Impact of horizontal spreading on light propagation through Arctic seasonal sea ice during melt pond progression, *J. Geophys. Res.*, *116*, C00G02, doi:10.1029/2010JC006908.

Eicken, H. (1992), Salinity profiles of Antarctic sea ice: Field data and model results, *J. Geophys. Res.*, *97*(C10), 15,545–15,557, doi:10.1029/92JC01588.

Eicken, H. (2003), From the microscopic, to the macroscopic, to the regional scale: Growth, microstructure and properties of sea ice, in *Sea Ice: An Introduction to its Physics, Chemistry, Biology, and Geology*, edited by D. N. Thomas and G. S. Dieckmann, pp. 22–81, Blackwell Sci, Oxford, U. K.

Fanning, K. A., and L. M. Torres (1991), ^{222}Rn and ^{226}Ra: Indicators of sea-ice effects on air-sea gas exchange, *Polar Res.*, *10*, 51–58, doi:10.1111/j.1751-8369.1991.tb00634.x.

Gao, H., and R. G. Zepp (1998), Factors influencing photoreactions of dissolved organic matter in a coastal river of the Southeastern United States, *Environ. Sci. Technol.*, *32*, 2940–2946, doi:10.1021/es9803660.

Garrison, D. L., and K. R. Buck (1986), Organism losses during ice melting: A serious bias in sea ice community studies, *Polar Biol.*, *6*, 237–239, doi:10.1007/BF00443401.

Giannelli, V., D. N. Thomas, C. Hass, G. Kattner, H. Kennedy, and G. S. Dieckmann (2001), Behaviour of dissolved organic matter and inorganic nutrients during experimental sea-ice formation, *Ann. Glaciol.*, *33*, 317–321, doi:10.3189/172756401781818572.

Gleitz, M., M. R. d. Loeff, D. N. Thomas, G. S. Dieckmann, and F. J. Millero (1995), Comparison of summer and winter inorganic carbon, oxygen and nutrient concentrations in Antarctic sea ice brine, *Mar. Chem.*, *51*, 81–91, doi:10.1016/0304-4203(95)00053-T.

Golden, K. M., S. F. Ackley, and V. I. Lytle (1998), The percolation phase transition in sea ice, *Science*, *282*, 2238–2241, doi:10.1126/science.282.5397.2238.

Gosink, T. A., J. G. Pearson, and J. J. Kelley (1976), Gas movement through sea ice, *Nature*, *263*, 41–42, doi:10.1038/263041a0.

Gosselin, M., M. Levasseur, P. A. Wheeler, R. A. Horner, and B. C. Booth (1997), New measurements of phytoplankton and ice algal production in the Arctic Ocean, *Deep Sea Res., Part II*, *44*, 1623–1644, doi:10.1016/S0967-0645(97)00054-4.

Gradinger, R. (2009), Sea-ice algae: Major contributors to primary production and algal biomass in the Chukchi and Beaufort Seas during May/June 2002, *Deep Sea Res., Part II*, *56*, 1201–1212, doi:10.1016/j.dsr2.2008.10.016.

Grannas, A. M., A. R. Bausch, and K. M. Mahanna (2007), Enhanced aqueous photochemical reaction rates after freezing, *J. Phys. Chem. A*, *111*, 11,043–11,049, doi:10.1021/jp073802q.

Gros, V., I. Peeken, K. Bluhm, E. Zöllner, R. Sarda-Esteve, and B. Bonsang (2009), Carbon monoxide emissions by phytoplankton: Evidence from laboratory experiments, *Environ. Chem.*, *6*, 369–379, doi:10.1071/EN09020.

Hellmer, H. H., C. Haas, G. S. Dieckmann, and M. Schröder (2006), Sea ice feedbacks observed in western Weddell Sea, *Eos Trans. AGU*, *87*(18), 173–184, doi:10.1029/2006EO180001.

Holm-Hansen, O., C. J. Lorenzen, R. W. Holmes, and J. D. Strickland (1965), Fluorometric determination of chlorophyll, *J. Cons. Cons. Int. Explor. Mer*, *30*, 3–15.

Horner, R. (1985), Taxonomy of sea ice microalgae, in *Sea Ice Biota*, edited by R. A. Horner, pp. 83–103, CRC Press, Boca Raton, Fla.

Kettle, A. J. (2005), Diurnal cycling of carbon monoxide (CO) in the upper ocean near Bermuda, *Ocean Modell.*, *8*, 337–367, doi:10.1016/j.ocemod.2004.01.003.

King, M. D., and C. F. Weber (2007), Distribution, diversity and ecology of aerobic CO-oxidizing bacteria, *Nat. Rev. Microbiol.*, *5*, 107–118, doi:10.1038/nrmicro1595.

King, M. D., J. L. France, F. N. Fisher, and H. J. Beine (2005), Measurement and modeling of UV radiation penetration and photolysis rates of nitrate and hydrogen peroxide in Antarctic sea ice: An estimate of the production rate of hydroxyl radicals in first-year sea ice, *J. Photochem. Photobiol. A*, *176*, 39–49, doi:10.1016/j.jphotochem.2005.08.032.

Klánová, J., P. Klán, D. Heger, and I. Holoubeka (2003), Comparison of the effects of UV, H_2O_2/UV and γ-irradiation processes on frozen and liquid water solutions of monochlorophenols, *Photochem. Photobiol. Sci.*, *2*, 1023–1031, doi:10.1039/b303483F.

Lavoie, D., R. W. Macdonald, and K. L. Denman (2009), Primary productivity and export fluxes on the Canadian shelf of the Beaufort Sea: A modeling study, *J. Mar. Syst.*, *75*, 17–32, doi:10.1016/j.jmarsys.2008.07.007.

Legendre, L., S. F. Ackley, G. S. Dieckmann, B. Gulliksen, R. Horner, T. Hoshiai, I. A. Melnikov, W. S. Reeburgh, M. Spindler, and C. W. Sullivan (1992), Ecology of sea ice biota. 2. Global significance, *Polar Biol.*, *12*, 429–444, doi:10.1007/BF00243114.

Loose, B., W. R. McGillis, P. Schlosser, D. Perovich, and T. Takahashi (2009), Effects of freezing, growth, and ice cover on gas transport processes in laboratory seawater experiments, *Geophys. Res. Lett.*, *36*, L05603, doi:10.1029/2008GL036318.

Loose, B., P. Schlosser, D. Perovich, D. Ringelberg, D. T. Ho, T. Takahashi, J. Richter-Menge, C. M. Reynolds, W. R. Mcgillis, and J.-L. Tison (2011), Gas diffusion through columnar laboratory sea ice: Implications for mixed-layer ventilation of CO_2 in the seasonal ice zone, *Tellus, Ser. B*, *63*, 23–39.

Miller, W. L., and R. G. Zepp (1995), Photochemical production of dissolved inorganic carbon from terrestrial organic-matter: Significance to the oceanic organic-carbon cycle, *Geophys. Res. Lett.*, *22*(4), 417–420, doi:10.1029/94GL03344.

Mopper, K., and D. J. Kieber (2000), Marine photochemistry and its impact on carbon cycling, in *The Effects of UV Radiation in the Marine Environ-*

ment, edited by S. de Mora, S. Demers, and M. Vernet, pp. 101–129, doi:10.1017/CBO9780511535444.005, Cambridge Univ. Press, New York.

Moran, M. A., and W. L. Miller (2007), Resourceful heterotrophs make the most of light in the coastal ocean, *Nat. Rev. Microbiol.*, *5*, 792–800, doi:10.1038/nrmicro1746.

Mundy, C. J., et al. (2011), Characteristics of two distinct high-light acclimated microbial communities during advanced stages of sea ice melt, *Polar Biol.*, doi:10.1007/s00300-011-0998-x, in press.

Parsons, T. R., Y. Maita, and C. M. Lalli (1984), *A Manual of Chemical and Biological Methods for Seawater Analysis*, Pergamon, New York.

Pursell, C. J., J. Conyers, P. Alapat, and R. Parveen (1995), Photochemistry of chlorine dioxide in ice, *J. Phys. Chem.*, *99*(26), 10,433–10,437, doi:10.1021/j100026a003.

Rachold, V., H. Eicken, V. V. Gordeev, M. N. Grigoriev, H.-W. Hubberten, A. P. Lisitzin, V. P. Shevchenko, and L. Schirrmeister (2004), Modern terrigenous organic carbon input to the Arctic Ocean, in *The Organic Carbon Cycle in the Arctic Ocean*, edited by R. Stein and R. W. Macdonald, pp. 33–55, Springer, New York, doi:10.1007/978-3-642-18912-8_2.

Riedel, A., C. Michel, M. Gosselin, and B. LeBlanc (2008), Winter–spring dynamics in sea-ice carbon cycling in the coastal Arctic Ocean, *J. Mar. Syst.*, *74*, 918–932, doi:10.1016/j.jmarsys.2008.01.003.

Różańska, M., M. Gosselin, M. Poulin, J. M. Wiktor, and C. Michel (2009), Influence of environmental factors on the development of bottom ice protist communities during the winter-spring transition, *Mar. Ecol. Prog. Ser.*, *386*, 43–59, doi:10.3354/meps08092.

Smith, R. E. H., M. Gosselin, S. Kudoh, B. Robineau, and S. Taguchi (1997), DOC and its relationship to algae in bottom ice communities, *J. Mar. Syst.*, *11*, 71–80, doi:10.1016/S0924-7963(96)00029-2.

Stubbins, A., G. Uher, C. S. Law, K. Mopper, C. Robinson, and R. C. Upstill-Goddard (2006), Open-ocean carbon monoxide photoproduction, *Deep Sea Res., Part II*, *53*, 1695–1705, doi:10.1016/j.dsr2.2006.05.011.

Swinnerton, J. W., and R. A. Lamontagne (1974), Carbon monoxide in the South Pacific Ocean, *Tellus*, *26*, 136–142, doi:10.1111/j.2153-3490.1974.tb01959.x.

Thompson, A. M. (1992), The oxidizing capacity of the Earth's atmosphere: Probable past and future changes, *Science*, *256*, 1157–1165, doi:10.1126/science.256.5060.1157.

Tison, J. L., A. Worby, B. Delille, F. Brabant, S. Papadimitriou, D. Thomas, J. de Jong, D. Lannuzel, and C. Haas (2008), Temporal evolution of decaying summer first-year sea ice in the Western Weddell Sea, Antarctic, *Deep Sea Res., Part II*, *55*, 975–987, doi:10.1016/j.dsr2.2007.12.021.

Tolli, J. D., and C. D. Taylor (2005), Biological CO oxidation in the Sargasso Sea and in Vineyard Sound, Massachusetts, *Limnol. Oceanogr.*, *50*(4), 1205–1212, doi:10.4319/lo.2005.50.4.1205.

Toyota, T., S. Takatsuji, K. Tateyama, K. Naoki, and K. I. Ohshima (2007), Properties of sea ice and overlying snow in the southern Sea of Okhotsk, *J. Oceanogr.*, *63*, 393–411, doi:10.1007/s10872-007-0037-2.

Wanninkhof, R. (1992), Relationship between wind speed and gas exchange over the ocean, *J. Geophys. Res.*, *97*(C5), 7373–7382, doi:10.1029/92JC00188.

Watson, R. T., H. Rodhe, H. Oeschger, and U. Siegenthaler (1990), Greenhouse gases and aerosols, in *Climate Change: The IPCC (Intergovernmental Panel on Climate Change) Scientific Assessment*, edited by J. T. Houghon, G. J. Jenkins, and J. J. Ephraums, pp. 1–40, Cambridge Univ. Press, New York.

Winther, J.-G., K. Edvardsen, S. Gerland, and B. Hamre (2004), Surface reflectance of sea ice and under-ice irradiance in Kongsfjorden, Svalbard, *Polar Res.*, *23*, 115–118, doi:10.1111/j.1751-8369.2004.tb00134.x.

Wiscombe, W. J., and S. G. Warren (1980), A model for the spectral albedo of snow. I: Pure snow, *J. Atmos. Sci.*, *37*(12), 2712–2733, doi:10.1175/1520-0469(1980)037<2712:AMFTSA>2.0.CO;2.

Xie, H., and M. Gosselin (2005), Photoproduction of carbon monoxide in first-year sea ice in Franklin Bay, southeastern Beaufort Sea, *Geophys. Res. Lett.*, *32*, L12606, doi:10.1029/2005GL022803.

Xie, H., and O. C. Zafiriou (2009), Evidence for significant photochemical production of carbon monoxide by particles in coastal and oligotrophic marine waters, *Geophys. Res. Lett.*, *36*, L23606, doi:10.1029/2009GL041158.

Xie, H., S. S. Andrews, W. R. Martin, J. Miller, L. Ziolkowski, C. D. Taylor, and O. C. Zafiriou (2002), Validated methods for sampling and headspace analysis of carbon monoxide in seawater, *Mar. Chem.*, *77*, 93–108, doi:10.1016/S0304-4203(01)00065-2.

Xie, H., O. C. Zafiriou, W.-J. Cai, R. G. Zepp, and Y. Wang (2004), Photooxidation and its effect on the carboxyl content of dissolved organic matter in two coastal rivers in the Southeastern United States, *Environ. Sci. Technol.*, *38*, 4113–4119, doi:10.1021/es035407t.

Xie, H., O. C. Zafiriou, T. P. Umile, and D. J. Kieber (2005), Biological consumption of carbon monoxide in Delaware Bay, NW Atlantic and Beaufort Sea, *Mar. Ecol. Prog. Ser.*, *290*, 1–14, doi:10.3354/meps290001.

Xie, H., S. Bélanger, S. Demers, W. F. Vincent, and T. N. Papakyriakou (2009a), Photobiogeochemical cycling of carbon monoxide in the southeastern Beaufort Sea in spring and autumn, *Limnol. Oceanogr.*, *54*(1), 234–249, doi:10.4319/lo.2009.54.1.0234.

Xie, H., Y. Zhang, K. Lemarchand, and P. Poulin (2009b), Microbial carbon monoxide uptake in the St. Lawrence estuarine system, *Mar. Ecol. Prog. Ser.*, *389*, 17–29, doi:10.3354/meps08175.

Zafiriou, O. C., S. S. Andrew, and W. Wang (2003), Concordant estimates of oceanic carbon monoxide source and sink processes in the Pacific yield a balanced global "blue-water" CO budget, *Global Biogeochem. Cycles*, *17*(1), 1015, doi:10.1029/2001GB001638.

Zafiriou, O. C., H. Xie, N. B. Nelson, R. Jajjar, and W. Wang (2008), Diel carbon monoxide cycling in the upper Sargasso Sea near Bermuda at the onset of spring and in mid-summer, *Limnol. Oceanogr.*, *53*(2), 835–850, doi:10.4319/lo.2008.53.2.0835.

Zhang, Y., H. Xie, C. G. Fichot, and G. Chen (2008), Dark production of carbon monoxide (CO) from dissolved organic matter in the St. Lawrence estuarine system: Implication for the global coastal and blue water CO budgets, *J. Geophys. Res.*, *113*, C12020, doi:10.1029/2008JC004811.

C. Aubry, Département de biologie et Centre d'études nordiques, Université Laval, Québec, QC G1V 0A6, Canada.

M. Gosselin, C. J. Mundy, B. Philippe, G. Song, and H. Xie, Institut des sciences de la mer de Rimouski, Université du Québec à Rimouski, 310 Allée des Ursulines, Rimouski, QC G5L 3A1, Canada. (huixiang_xie@uqar.qc.ca)

T. N. Papakyriakou, Centre for Earth Observation Science, Department of Environment and Geography, 470 Wallace Bldg., 125 Dysart Rd., University of Manitoba, Winnipeg, MB R3T 2N2, Canada.

Y. Zhang, Key Laboratory of Coastal Zone Environmental Processes, Yantai Institute of Coastal Zone Research, Chinese Academy of Sciences, Yantai, Shandong 264003, China.